Optofluidic membrane interferometer: An imaging method for measuring microfluidic pressure and flow rate simultaneously on a chip

Wuzhou Song and Demetri Psaltis
School of Engineering, Swiss Federal Institute of Technology Lausanne (EPFL),
CH-1015 Lausanne, Switzerland

We present a novel image-based method to measure the on-chip microfluidic pressure and flow rate simultaneously by using the integrated optofluidic membrane interferometers (OMIs). The device was constructed with two layers of structured polydimethylsiloxane (PDMS) on a glass substrate by multilayer soft lithography. The OMI consists of a flexible air-gap optical cavity which upon illumination by monochromatic light generates interference patterns that depends on the pressure. These interference patterns were captured with a microscope and analyzed by computer based on a pattern recognition algorithm. Compared with the previous techniques for pressure sensing, this method offers several advantages including low cost, simple fabrication, large dynamic range, and high sensitivity. For pressure sensing, we demonstrate a dynamic range of 0-10 psi with an accuracy of $\pm 2\%$ of full scale. Since multiple OMIs can be integrated into a single chip for detecting pressures at multiple locations simultaneously, we also demonstrated a microfluidic flow sensing by measuring the differential pressure along a channel. Thanks to the simple fabrication that is compatible with normal microfluidics, such OMIs can be easily integrated into other microfluidic systems for *in situ* fluid monitoring. © *2011 American Institute of Physics*. [doi:10.1063/1.3664693]

I. INTRODUCTION

As a fast-growing field, microfluidics and lab on chip systems have found numerous applications in the areas of biochemical detection, analysis, synthesis, and separations.[1–4] Accurate pressure monitoring is crucial for the precise control of as the pressure which is directly related to flow in microfluidic system. For an example, precisely regulated pressure was utilized to generate a continuous profusion of nutrient media for cell culture on chip.[5] Instead of delivering of chemical reagent, pressure driven flow can also handle the biological sample. For an example, pressure driven flow was utilized to scan the *Caenorhabditis elegans* in a chip-scale optofluidic microscopy (OFM) device.[6] In addition, pressure measurement has been also used for the characterization of the mechanical properties in microfluidic systems, such as liquid viscosity,[7] red blood cell deformability,[8] and hydrodynamic resistance of a single confined moving droplet in microfluidic channels.[9]

Most current pressure measurements still rely on external pressure transducers.[10,11] However, due to the pressure dissipation and delay in transmission, it is difficult to accurately measure the local pressure in a microfluidic system using an external pressure sensor. Thus the integration of pressure sensors into microfluidic chip could be desirable for *in situ* pressure measurement. To this end, several microfluidic pressure sensors have been demonstrated. Srivastava and Burns reported a pressure sensor based on monitoring the movement of a liquid-air interface where the trapped air is compressed in a sealed chamber.[12] But the material of devices is limited to non-gas-permeable material which is not compatible to the normal polydimethylsiloxane (PDMS) based microfluidic chip. Another method reported by Abkarian *et al.* is based on monitoring the position of the interface between the test liquid and the reference liquid in the comparator channel.[8] This method requires a continuous flow of the test liquid and cannot

measure the absolute pressure. Recently, Chung reported an image-based method to measure the pressure in microsystems by detecting the volume displacement of fluorescent particle suspensions.[13] This method is simple to implement but the accuracy can be influenced by the variation of focus depth or the non-uniform distribution of the fluorescent particles.

Meanwhile, in-line microfluidic flow sensing is also desirable for precise flow control for lab-on-a-chip applications. Several types of microfluidic flow sensor were developed in the past. For an example, flow sensor, that is, based on sensing the temperature difference between two adjacent points in a micro-channel had been reported by Ernst *et al.*[14] Such flow sensors require complex fabrication to integrate heater and temperature sensors. Collins and Lee reported a microfluidic flow transducer based on measuring the electrical admittance of fluid.[15] However, this method is not applicable to the conductive fluid. Lien and Vollmer reported a microfluidic flow sensor based on integrated optical fiber cantilever, but it also requires complicated fabrication and packaging process.[16]

As an emerging field, optofluidics has enabled a number of novel optical functional devices built on microfluidic systems,[17–23] such as optofluidic lens,[24] light sources,[25–27] molecule sensors,[28] interferometers,[29,30] optofluidic prism,[31] and color filter.[32] Different from the normal on-chip interferometer that requires optical fibers and complicated package.[29,33] Recently, we induced the imaging based interferometer integrated on chip based on the mechanism of localized thin film interference.[34,35] In this work, we demonstrated a versatile imaging based method for simultaneously determining the microfluidic pressure and flow rate on a chip with the integrated optofluidic membrane interferometers (OMIs). In this device, the pressure is directly measured by the OMI, which consists of a flexible air-gap optical cavity which generates interference patterns upon illumination by monochromatic light. Meanwhile, two identical OMIs combined with a simple microfluidic circuit compose a differential pressure flow meter. The whole sensing unit was integrated inside the chip with a small footprint. As the fabrication of the device is fully compatible with conventional PDMS based microfluidic chip; the sensing unit is ready to integrate into the other microfluidic chip for *in situ* pressure and flow rate measurement. Thanks to the interferometric method and the image processing algorithm, this method offers multiple advantages including high accuracy, large dynamic range, and good reliability.

II. WORKING PRINCIPLE OF OMI

The OMI was integrated in an optofluidic chip and monitored on a microscope. The schematic of the whole apparatus is shown in Figure 1. The chip was illuminated by a
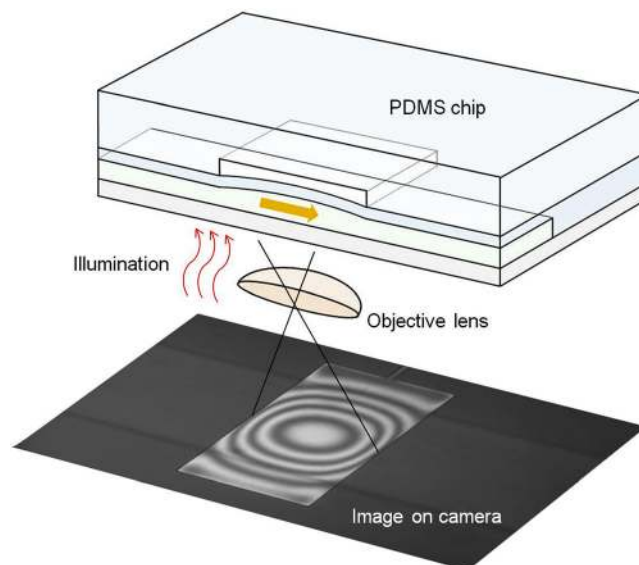

FIG. 1. The schematic of whole apparatus for pressure measurement with OMI.
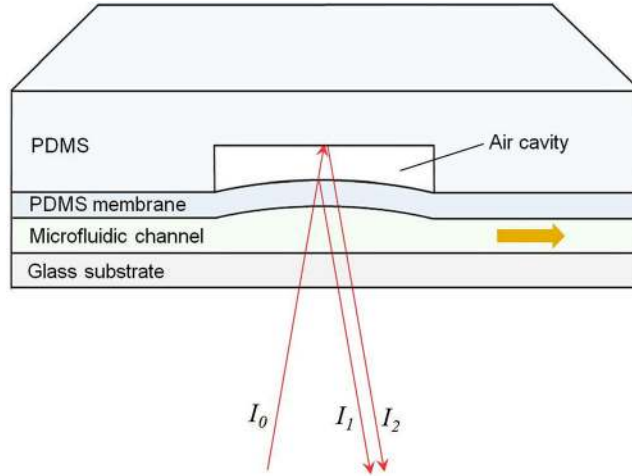
FIG. 2. The structure of the OMI which contains a glass substrate, and two layers of PDMS.

monochromatic diffuse light source. The image of the interference pattern from the OMI was projected onto a digital camera through an objective lens on the microscope. The pressure value was then obtained by analyzing these interference patterns. The chip was made of PDMS, which was bonded onto a glass slide. As shown in Figure 2, the chip consists of two layers of structured PDMS layers on top of a glass substrate. The liquid flows inside a microfluidic channel formed between the glass substrate and the bottom layer of PDMS. Above the microfluidic channel, there is an air-gap chamber sandwiched between the two PDMS layers, where the bottom layer of PDMS functions as an elastic membrane for pressure transducing. The OMI mainly consists of microfluidic channel, PDMS membrane, and an air-gap cavity. A temporal coherent light goes through the microfluidic channel and illuminates the air-gap cavity illuminates the chip. The reflected light from the two air-gap interferes inside the cavity interferes with each other constructively or destructively, depending on the air-gap thickness. The resulting total reflection intensity can be expressed as

$$I = I_1 + I_2 + 2\sqrt{I_1 I_2}\cos\phi, \tag{1}$$

where I_1 and I_2 are the reflection intensities from the bottom and top PDMS-air boundaries, respectively. Assuming the incident intensity at the bottom PDMS-air boundary is I_0, due to the low reflectivity on these two boundaries, we have $I_1 \approx I_2 \approx I_0 \times 4\%$, here, the PDMS has a refractive index of 1.412. Thus, multiple reflections can be neglected in this model. Meanwhile, nice image contrast can be obtained due to $I_1 \approx I_2$. Note that there also exist reflections at the boundaries of PDMS-liquid and glass-liquid. However, the reflection there is much lower than the one of the PDMS-air boundary. The phase difference ϕ between the two reflection beams depends on the air gap distance d

$$\phi = \frac{4d\pi}{\lambda} + \pi, \tag{2}$$

where λ is the wavelength of incidence light. When the fluids inside microfluidic channels are subjected to a pressure, the PDMS membrane is deformed to a convex shape towards the air-gap. Due to the thickness variation of the air-gap, the air gap cavity presents an interference pattern, which reflects the pressure of the fluid. A digital camera on the microscope captures these interference patterns.

III. EXPERIMENTS

A. Device fabrications

The optofluidic chip was fabricated by multilayer soft lithography (MSL), which has been widely utilized to make the membrane valves and pumps on microfluidic devices.[36] The two PDMS layers were replicated from two different master molds that were patterned by standard UV lithography. The mold for the bottom layer of PDMS film was defined on a 50 μm thickness of SU-8 (Gersteltec, Switzerland). The width of the microfluidic channel underneath the bottom layer is 400 μm. The molds were treated with trimethylchlorosilane vapor (TMS, Sigma Aldrich). A monomer for PDMS membrane was prepared by mixing the prepolymer components in 10:1 ratio (base: curing agent, Dow Corning Sylgard 184). The bottom layer of PDMS should be thin enough since it works as a flexible membrane for pressure sensing. Meanwhile, the surface of the PDMS membrane should be flat to get the nice interference pattern. To fabricate such thin PDMS layer with smooth surface, we put several small pieces of silicon wafer around the edge of the wafer which contains the SU-8 mold. These small silicon pieces functioned as the spacer to fix the thickness of the PDMS membrane. After dispensing the PDMS prepolymer onto the SU-8 mold, the mold was covered by another blank wafer which was then slightly pressed by loading a weight. The wafer was coated with a layer of Chrome for anti-sticking between PDMS and wafer. After the PDMS prepolymer was cured in an oven, the PDMS membrane was carefully separated from the SU-8 mold and blank wafer. The PDMS membrane was then cut into the required size and transferred to another clean silicon substrate. The thickness of the PDMS membrane was measured on microscope by imaging its cross-section. The thickness of the PDMS membrane is 530 μm in this paper otherwise stated. The top PDMS layer of the chip was also prepared by replica molding from a SU8 mold which has a thickness of 20 μm. This PDMS layer has a thickness of 4 mm. Figure 3 shows the entire fabrication process; the two PDMS layers were treated by oxygen plasma (12 W, 20 s) and then bonded together on a homemade aligning setup. After drilling the holes, the bonded PDMS part was then bonded onto a glass substrate via oxygen plasma. The chip was finally baked in the oven at 100 °C for more than 24 h to ensure the bonding strength. The Young's modulus of the PDMS was expected to be 4 MPa according to the literature.[37]
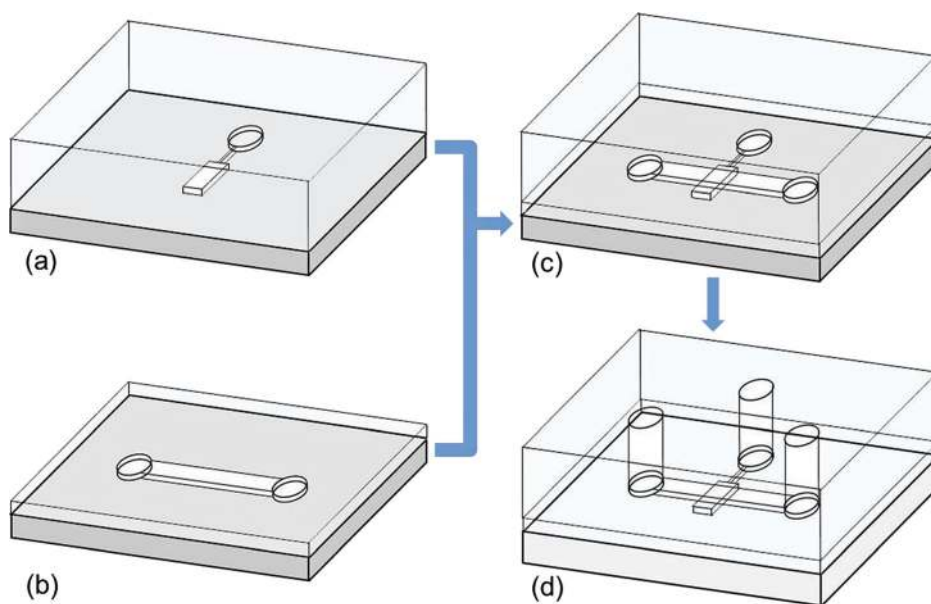

FIG. 3. The fabrication process of the OMI.

B. Measurement setup

The chip was measured with a bright field microscope (Infinity Microscope and Mitutoyo M Plan Apo 5 × objective) with a built-in beam splitter for illumination. The light source was a broadband light source (Dolan-Jenner, PL-800 Illuminator with tungsten lamp inside) added with a laser line filter (Thorlabs, FL632.8-1) that has a transmission line-width 1 nm. This monochromatic light source has sufficient temporal coherence to obtain high quality interference pattern without the speckle noise. Notice that the illumination onto the chip is a diffuse light source without spatial coherence. Due to the nature of thin film interference, we found the optical setup did not require very critical optical adjustment or alignment to get high quality of inference pattern, as long as the air-gap cavity was closed to the focal plane of the microscope. The image was recorded by a monocolor CCD camera (Scion, CFW-1312 M). The pressure was generated from a precise mechanical air pressure regulator (100-AB, Air Control, Inc.) And calibrated with a digital pressure gauge (Omega DPG4000). For the pressure measurement, the chip was connected with a tube and filled with pure water which was driven by the compressed air. In the microfluidic flow measurement, three types of liquids were used: water, 10% and 20% (by weight) glycerol in water solution (Sigma). The liquid flow was generated on a programmable syringe pump (New Era Pump Systems, Wantagh, NY). A disposable syringe containing the liquid was directly connected to the microfluidic chip through Tygon tubing. All the image analysis and calculation were done on commercial MATLAB software.

IV. RESULTS AND DISCUSSION

A. Pressure measurement

Figure 4 shows an example image of interference pattern at 5.5 psi of pressure taken on the microscope. The air-gap cavity has a rectangular shape with a size of $200 \, \mu m \times 480 \, \mu m$. A small channel at the bottom connects the air-gap cavity with a vent hole to keep the pressure inside the cavity be equal to the ambient air. Notice that all the pressure in this paper represents the relative pressure to the ambient air. The interference patterns consist of several dark and bright concentric rings that move in or out upon the pressure decrease or increase. The microfluidic channel underneath the cavity is also visible. Compared with the cavity, the background area around the cavity is much darker due to the relative low reflectivity at the PDMS-liquid
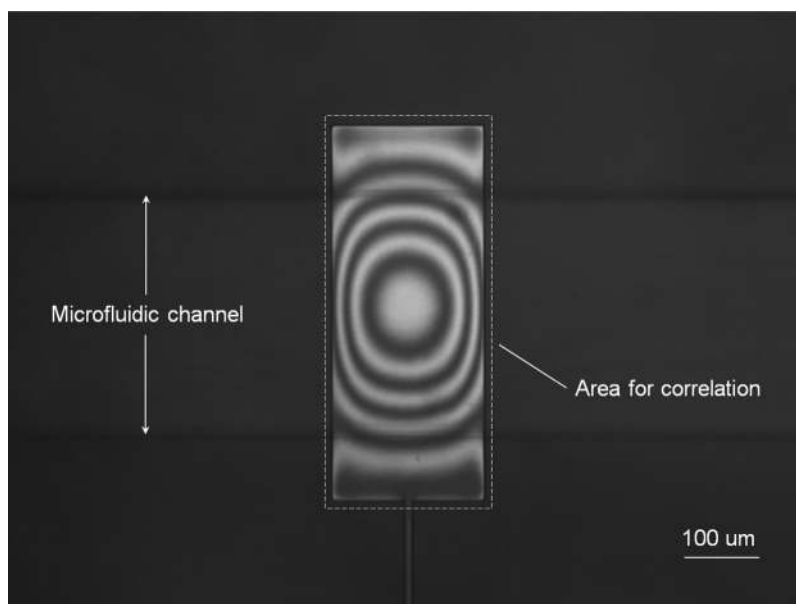

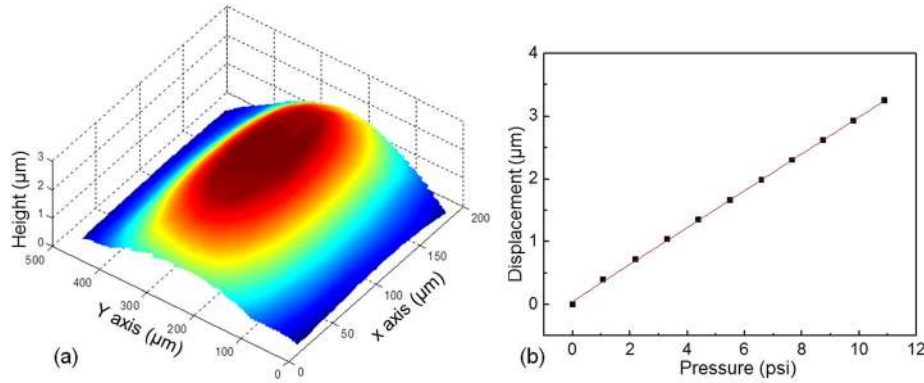FIG. 4. An example of the interference pattern at 6.5 psi captured under microscope.

FIG. 5. (a) The membrane shape deduced from the interference pattern at 6.5 psi. (b) The displacement of the membrane in center area versus the pressure.

and glass-liquid interfaces. For an example, here, the refractive indexes contrast of PDMS to water is 1.41/1.33; hence, the reflection coefficient is calculated to be 0.09% that is much lower than the value of 3% at PDMS-air boundary. From the interference pattern in Figure 4, based on Eqs. (1) and (2), the shape of the membrane surface was calculated and is shown in Figure 5(a). From the interference pattern, the displacement in the center area of the membrane was also calculated. Figure 5(b) shows the plot of displacement versus the pressure which gives a nicely linear relation. From the slope of the fitting line, the pressure sensitivity of this sensor is calculated to be 0.30 μm/psi. As the air-gap cavity has a height of about 20 μm, thus, we estimate that the membrane would touch the opposite side of the cavity at the pressure of larger than 66 psi, which exceeds the upper limit of the pressure source we have.

To calculate the pressure value from the recorded interference patterns, we induced an image correlation method to analyze such holographic fringes. As each pressure level corresponds to a specific interference image, we compare the measured image to a database which contains a batch of the reference images with known pressure value that were obtained during the calibrations. The measured pressure value is determined by which among the reference images gives the best fit to the measured image. To find the most matching images, we adopted the Pearson's correlation coefficient to quantitatively characterize the similarity between two (grayscale) images, as presented in the following equation[38]:

$$r = \frac{\sum_i (A_i - A_m)(B_i - B_m)}{\sqrt{\sum_i (A_i - A_m)^2} \sqrt{\sum_i (B_i - B_m)^2}}, \tag{3}$$

where A_i is the intensity of the ith pixel in image A, B_i is the intensity of the ith pixel in image B, A_m is the mean intensity of image A, and B_m is the mean intensity of image B. The correlation coefficient has the value $r = 1$ if the two images are absolutely identical, $r = 0$ if they are completely uncorrelated. In this work, firstly, we calibrated the pressure sensor chip with the digital gauge from 0 to 10 psi at 0.1 psi intervals. At each pressure point during calibration, we took one picture as a reference image. As the intensity of each pixel on the image varies continuously within the calibration interval in terms of pressure, it is possible to add many more reference images by interpolating from the nearby reference images. The interpolation can significantly alleviate the calibration work; meanwhile, it can enhance the measurement resolution. Figure 6 gives an example of such an interpolation between nearby reference images at pressure of 6.8 and 6.9 psi. After interpolation, the total number of reference images was increased to 10 times to the original one. In order to enhance the accuracy, a third order polynomial (cubic spline) interpolation was employed.[39] Thus, each interval image is the computational result of nearby four images directly obtained from calibration.
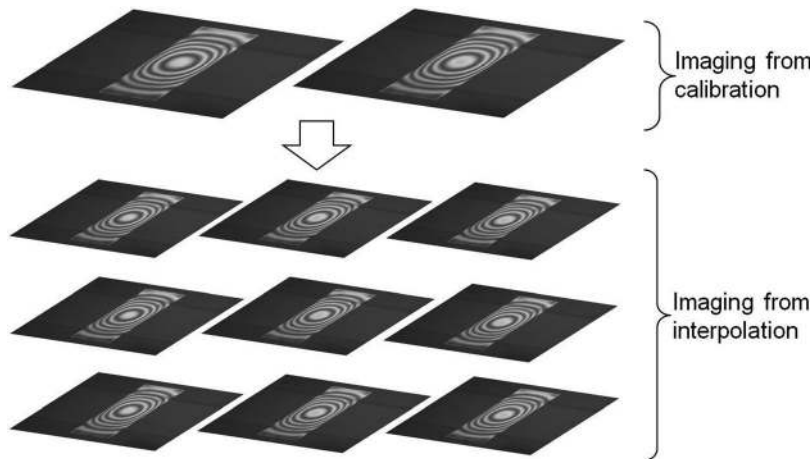
FIG. 6. The Schematic of the image interpolation between the pressure of 6.8 and 6.9 psi.

Figure 7 shows the measured results at five different points in the range of 0-10 psi. The insets are the interference patterns corresponding to each pressure labeled nearby. The horizontal coordinate represents the pressure value of each reference image, while the vertical coordinate represents the correlation coefficient between the measuring image and the reference images. To eliminate the influence from the area surrounding the cavity, we cropped all the images before calculating the correlation coefficient. The area is indicated by the square of dashed-line in Figure 5. The correlation area for calculation has a size of 228 pixels $\times$ 516 pixels. This image correlation recognition method was proved to work well as we can see that the maximum peak on each curve can be easily discriminated and their values at these peaks almost reach 1. Thus, the measured pressure is determined by the x coordinate of the maximum peak on this plot. Note that as the image correlation is based on the evaluation of an entire image, the pressure measurement is still realizable even there exist the tiny defects or dusts inside the OMI cavity.
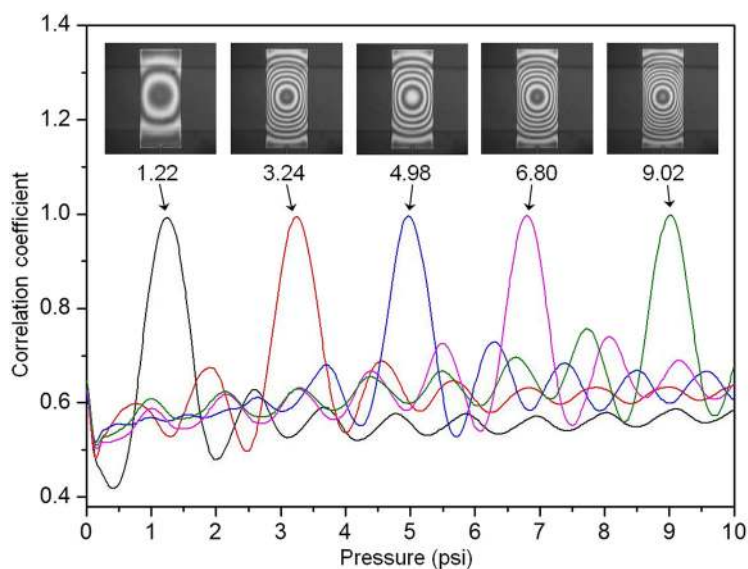

FIG. 7. The plot of the correlation coefficient against the pressure of reference images. The insets show the images at the corresponding pressures. The numbers are the measured pressure values obtained from the horizontal position of these maximum peaks.

When the pressure sensor is subjected to negative pressure, the membrane surface in the air-gap cavity side will deform into a concave instead of convex shape at positive pressure. Due to the symmetry, the interference pattern may look similar in both conditions. Thus, the working range of this device is only allowed to be above 0 psi. We also found the image correlation method is still effective and accurate even at very low pressure when the interference pattern becomes almost flat without fringes. The upper limit of the working range can extend to the point when the air-gap cavity begins to collapse. The working range of this pressure sensor can extend to more than 40 psi which already exceeds the upper limit range of the air pressure regulator in this experiment. In this work, we did the calibration and measurement in the range of 0-10 psi, which was considered as the working range. Another possible factor that limits the working range is the image resolution of the correlation area. When the pressure is too high, the fringes become too dense and the camera may no longer be able to distinguish them if the image resolution is too low. We stimulated different image sizes of the correlation area by numerically scaling the image. The original image size of the correlation area is 228 pixels $\times$ 516 pixels. We find even image size is reduced by a factor of 5, it is still sufficient to determine the pressure in the whole working range of 0-10 psi. During the experiment, we found too large thickness of the air-gap cavity can significantly degrade the image quality of the interference pattern. In theory, to get clear interference pattern, the air-gap thickness should be within the coherence length of the light source and the depth of focus of the microscope. To get clear interference pattern, the wavefronts of two reflections that are projected onto the image plane from the cavity should be temporal coherent each other and without being blurred. From the testing we have done, the maximum of cavity thickness is about 50 μm that still allows getting a decent interference pattern. For a fixed air-gap thickness, the working range can be chosen by adjusting the thickness of the PDMS membrane or the size of the cavity. The thinner PDMS membrane means high sensitivity and less working range and vice-versa. Figure 8(a) shows the dependence of pressure sensitivity on the membrane thickness from experiment.

We investigated the accuracy of the device by comparing the measured value to the digital gauge. For each pressure condition, the measurements were repeated at least 6 times from different previous state. Figure 8(b) shows accuracy distribution in the working range of 0-10 psi. Here, the error bars are the standard deviations of the measurements obtained from five sampling. From the graph, pressure accuracy is estimated to be about $\pm 2\%$ of full scale. During the measurement, we also noticed that the pressure errors were related to the previous states; especially many different pressures were applied for a long time at previous states. This was interpreted as the result of shape memory effect of the PDMS membrane.

During the characterization, we also found that no critical alignment was required to obtain a nice interference pattern as long as the microscope focused well. The interference pattern of OMI was insensitive to the vibration or illumination condition. We also tested this device on a normal inverted research microscope (Olympus IX71, Japan) by modifying one of filter cubes. We replaced the original excitation filter with a laser line filter (Thorlabs, FL632.8-1), replacing
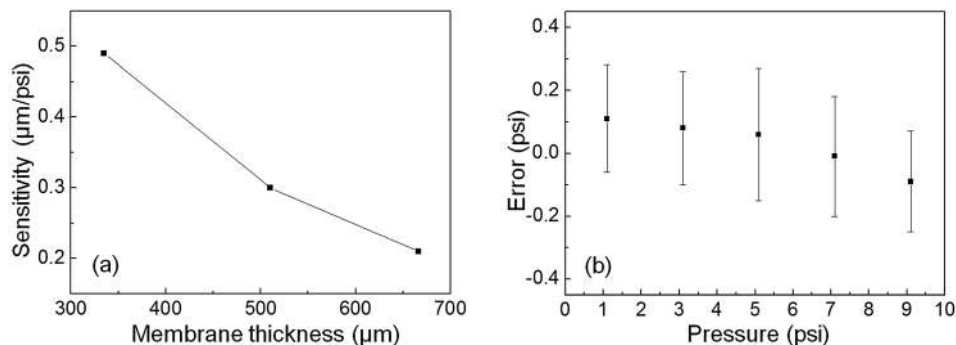

FIG. 8. (a) The sensitivity of the pressure sensor versus the membrane thickness. (b) The distribution of measurement error at different pressure range.

the dichroic mirror with a piece of glass slide as a simple beam splitter and removing the emission filter. The chip was monitored under a low magnification objective ($5\times$) in the epifluorescent configuration. We found that the interference pattern from the OMI cavity in this case had very similar quality to the ones shown in the Figure 7.

B. Microfluidic flow rate measurement

In addition to the pressure sensing, a differential pressure based microfluidic flow-meter was also demonstrated by integrating such two OMIs with a microfluidic circuit on a single chip. The flow rate is calculated from the pressure drop induced by the flow along a narrow microfluidic channel. Figure 9 shows an example picture of the device captured on the microscope. Two OMIs are located at the two ends of the middle microfluidic channel for measuring the pressures of up and down stream, respectively. The two OMIs have the same dimensions as presented in the above section. The narrow microfluidic channel in the center has a length of about $530\,\mu m$ and a rectangular cross-sectional shape with the size of $30\,\mu m \times 20\,\mu m$ (width $\times$ height). For a steady laminar flow in a rectangular channel with constant cross-sectional areas, the pressure gradient is linearly proportional to the flow rate Q,[40]

$$-\frac{\partial p(z)}{\partial z} = \frac{12\mu}{h^3 W}Q,$$ (4)

where $p(z)$ is the pressure along the position z, μ is the fluid viscosity, W is the channel width, and h is the channel height. As the flow rate along the whole microfluidic channel is constant, the total pressure drop ΔP between these two pressure sensors can be obtained shown Eq. (4) as shown below,

$$\Delta P = -\int \frac{12\mu}{h^3 W}\partial z \cdot Q.$$ (5)

From the fact that the differential pressure ΔP across the microfluidic channel is linearly proportional to the flow rate Q, experimentally, we can calculate the flow rate Q from the following equation:

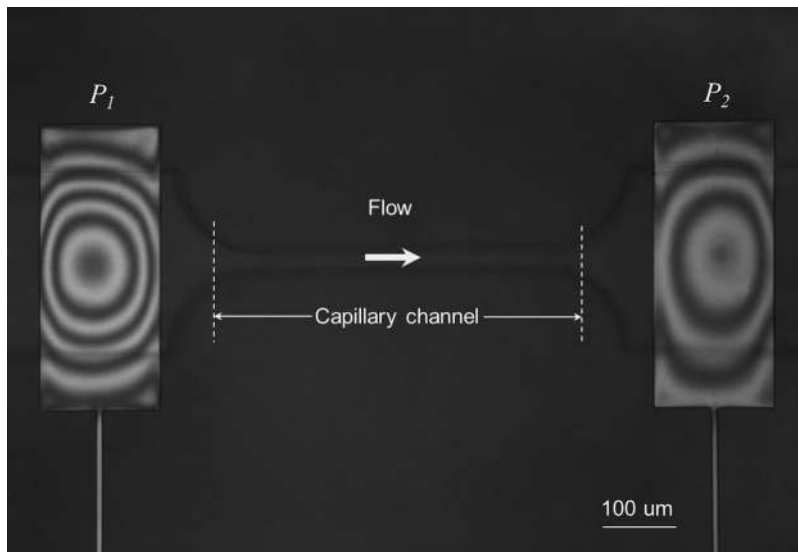$$Q = k\Delta P = k(P_1 - P_2),$$ (6)

FIG. 9. An example image of the flow meter which contains two OMIs for pressure sensing at up (P_1) and downstream (P_2).
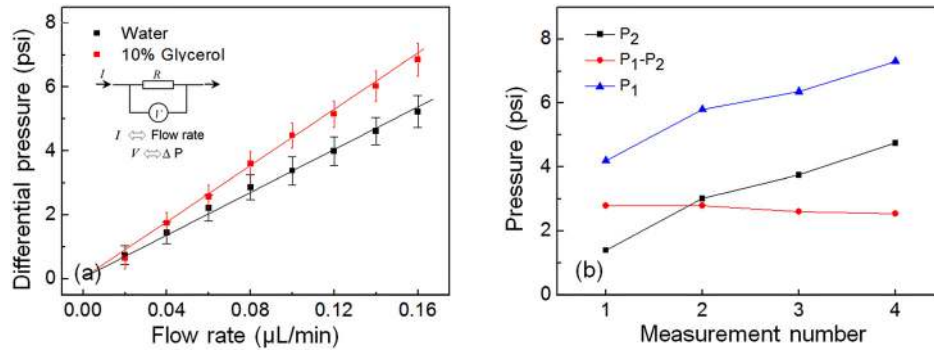
FIG. 10. (a) The plot of the differential pressure (P2-P1) versus the flow rate for water and 10% glycerol solution. (b) The measurement results (P_1, P_2 and P_1-P_2) for a constant flow of 0.08 μl/min at the condition of different outlet pressure.

where k is a constant coefficient which can be obtained from calibration; P_1 and P_2 are the upstream and downstream pressure, respectively.

Figure 10(a) shows the measured differential pressures ΔP in response to various flow rates Q of the two different liquids. The inset figure shows a resistant electrical circuit as an equivalent model for this flow meter. Here, the electrical current equivalents to the flow rate; the voltage equivalents to the differential pressure. The two differential liquids include the water and glycerol-water solutions (10% in weight percent) with varying viscosity. The error bars are the standard deviations of ΔP obtained from five measurements with time intervals of 3 min. For each liquid, we can see a nice linear relationship between the flow rates and the differential pressures. The lines can fit the data points very well and each liquid corresponds to the lines with different slope rate. For a constant flow rate, if the fluid resistances at the outlet of the flow meter are different, we will get different sets of pressure values that may result different differential pressure. To investigate such effect on the flow rate measurement, we chose the water as the sample liquid, set a constant flow rate of 0.08 μl/min. The outlet fluid resistance was adjusted by squeezing the tubing connected to the flow meter chip. When the outlet resistance increases, both the upstream and downstream pressure will increase. The experimental results are shown in Figure 10(b). The horizontal coordinate represents different measurements with increasing outlet resistance. The square and triangular dots indicate the upstream and downstream pressure, respectively; the circle dots are the calculated differential pressures. From the figure, we can see that the differential pressure slightly decreases with the overall pressure increment. This may be explained that the cross-section of microfluidic channel expands when the overall pressure increases due to the elastic property of the PDMS.[41]

From above flow measurement, we can determine the coefficient value of k for each liquid. Thus for the practical flow rate measurement of the same liquid, the flow rate can be simply calculated by multiplying the differential pressure ΔP with k. For this device, we calculated the k values are 0.0297 and 0.0227 μlmin^{-1}psi^{-1} for water and 10% glycerol-water solution, respectively. From the calibration results shown in Figure 10(a), we estimate the flow rate measurement on water has an accuracy of $\pm$ 5% of full scale in the working range of 0-0.16 μl/min. We also noticed that the k values are associated with the viscosities of each liquid with a linear relationship. The viscosities μ (obtained from literature) for water and 10% glycerol solution are 1.005 and 1.310, respectively, at temperature of 20 $^\circ$C. The fact of that the coefficient of k/μ are almost same is in agreement with Eq. (5). Hence, this device can be also utilized to measure the liquid viscosity if the flow rate is known.

V. CONCLUSIONS

We develop an optical interferometric method for measuring both the microfluidic pressure and flow rate simultaneously on a chip based on the integrated OMIs. The measurement was

realized by imaging the interference pattern from the cavity of OMI under a microscope upon monochromatic illumination. The device was fabricated with multilayer soft-lithograph, which is low cost and can be easily migrated into other microfluidic system. Due to the nature of localized interference, the interference pattern can be insensitive to vibration or illumination condition. As long as the microscope focuses well, the nice interference pattern can be obtained without additional alignment. To analyze the interference pattern, we also presented an imaging correlation method, which was proved to be highly reliable. Thanks to such optical interferometry method, the OMI shows high accuracy for pressure measurement. The sensitivity and working range for the pressure sensing can be chosen by adjusting the membrane thickness or the size of OMI cavity. The working range of the flow rate measurement can be also varied by properly designing the microfluidic resistance channel in between the two pressure sensors. Since each of the OMIs has small size, multiplex pressure and flow measurement in spatial on a single chip can be easily achieved by integrating multiple of such OMIs. In addition, with the integration of such OMIs into the other microfluidic system, the imaging method could allow simultaneous monitoring of the pressure and flow rate in channels, as well as the dynamic of the fluid or biochemical reactions that could be desirable for microfluidics and biology community.

[1] S. Mandal, J. Goddard, and D. Erickson, Lab Chip **9**, 2924 (2009).
[2] G. M. Whitesides, Nature (London) **442**, 368 (2006).
[3] D. Dendukuri, S. S. Gu, D. C. Pregibon, T. Alan Hatton, and P. S. Doyle, Lab Chip **7**, 818 (2007).
[4] Z. Wu, B. Willing, J. Bjerketorp, J. K. Jansson, and K. Hjort, Lab Chip, **9**, 1193 (2009).
[5] H. Hufnagel, A. Huebner, C. Gülch, K. Güse, C. Abell, and F. Hollfelder, Lab Chip **9**, 1576 (2009).
[6] X. Cui, L. M. Lee, X. Heng, W. Zhong, P. W. Sternberg§, D. Psaltis, and C. Yang, Proc. Natl. Acad. Sci. U. S. A. **105**, 10670 (2008).
[7] S. Choi and J. K. Park, Small **6**, 1306 (2010).
[8] M. Abkarian, M. Faivre, and H. A. Stone, Proc. Natl. Acad. Sci. U. S. A. **103**, 538 (2006).
[9] M. J. Fuerstman, A. Lai, M. E. Thurlow, S. S. Shevkoplyas, H. A. Stone, and G. M. Whitesides, Lab Chip **7**, 1479 (2007).
[10] B. Kuczenski, P. R. LeDuc, and W. C. Messner, Lab Chip **7**, 647 (2007).
[11] G. Chen, F. Svecb, and D. R. Knappa, Lab Chip **8**, 1198 (2008).
[12] N. Srivastava and M. A. Burns, Lab Chip **7**, 633 (2007).
[13] K. Chung, H. Lee, and H. Lu, Lab Chip **9**, 3345 (2009).
[14] H. Ernst, A. Jachimowicz, and G. A. Urban, Sens. Actuators, A. **100**, 54 (2002).
[15] J. Collins and A. P. Lee, Lab Chip **4**, 7 (2004).
[16] V. Lien and F. Vollmer, Lab Chip **7**, 1352 (2007).
[17] D. Psaltis, S. R. Quake, and C. Yang, Nature (London) **442**, 381 (2006).
[18] V. R. Horowitz, D. D. Awschalom, and Sumita Pennathur, Lab Chip **8**, 1856 (2008).
[19] Y. Yang, A. Q. Liu, L. Lei,L. K. Chin, C. D. Ohl, Q. J. Wang, and H. S. Yoon, Lab Chip **11**, 3182 (2011).
[20] S. Xiong, A. Q. Liu, L. K. Chin, and Y. Yang, Lab Chip **11**, 1864 (2011).
[21] Z. G. Li, Y. Yang, X. M. Zhang, A. Q. Liu, J. B. Zhang, L. Cheng, and Z. H. Li, Biomicrofluidics **4**, 043013 (2010).
[22] L. K. Chin, A. Q. Liu, Y. C. Soh, C. S. Lim, and C. L. Lin, Lab Chip **10**, 1072 (2010).
[23] W. Song and D. Psaltis, Lab Chip **11**, 2397 (2011).
[24] X. Mao, S. S. Lin, M. I. Lapsley, J. Shi, B. K. Juluri, and T. J. Huang, Lab Chip **9**, 2050 (2009).
[25] W. Song and D. Psaltis, Appl. Phys. Lett. **96**, 081101 (2010).
[26] W. Song, A. E. Vasdekis, Z. Li, and D. Psaltis, Appl. Phys. Lett. **94**, 051117 (2009).
[27] W. Song, A. E. Vasdekis, Z. Li, and D. Psaltis, Appl. Phys. Lett. **96**, 081101 (2010).
[28] H. Li and X. Fan, Appl. Phys. Lett. **97**, 011105 (2010).
[29] W. Z. Song, X. M. Zhang, A. Q. Liu, P. H. Yap, and H. Hosseini, Appl. Phys. Lett. **89**, 203901 (2006).
[30] W. Z. Song, A. Q. Liu, S. Swaminathan, C. S. Lim, P. H. Yap, and T. C. Ayi, Appl. Phys. Lett. **99**, 223902 (2007).
[31] S. Xiong, A. Q. Liu, L. K. Chin, and Y. Yang, Lab Chip **11**, 1864 (2011).
[32] A, Llobera, S. Demming, H.N. Joensson, V. J. Vila-Planas, H. Andersson-Svahn, and S. Buttgenbach. Lab Chip **10**, 1987 (2010).
[33] P. Domachuk, I. C. M. Littler, M. Cronin-Golomb, and B. J. Eggletona, Appl. Phys. Lett. **88**, 093513 (2006).
[34] W. Song and D. Psaltis, Optics Exp. **18**, 16561 (2010).
[35] W. Song and D. Psaltis, Optics Lett. **35**,3604 (2010).
[36] M. A. Unger, H. Chou, T. Thorsen, A. Scherer, and S. R. Quake, Science **288**, 113 (2000).
[37] D. Fuard, T. Tzvetkova-Chevolleau, S. Decossas, P. Tracqui, and P. Schiavone, Microelectron. Eng. **85**, 1289 (2008).
[38] J. L. Rodgers and W. A. Nicewander, Am. Stat. **42**, 59 (1988).
[39] C. Boor, *A Practical Guide to Splines* (Springer-Verlag, New York, 2001).
[40] J. Happel and H. Brenner, *Low Reynolds Number Hydrodynamics* (Prentice-Hall, New York, 1965) p. 34.
[41] B. S. Hardy, K. Uechi, J. Zhen, and H. P. Kavehpour, Lab Chip **9**, 935 (2009).